PCCP

Check for updates

Variation of topological surface states of nodal line semimetal MgB₂ resulting from adsorption of hydrogen, hydroxide, and water molecules†

Pangdong Zhu,[a] Kun Bu,*[b] Ruzhi Wang [ID] [a] and Changhao Wang [ID] *[a]

Topological semimetals have garnered significant interest due to their intrinsic topological physics and potential applications in devices. A crucial feature shared by all topological materials is the bulk-boundary correspondence, indicating the presence of unique topologically protected conducting states at the edges when non-trivial band topology exists in the bulk. Previous studies on surface states of topological materials predominantly focused on pristine surfaces, leaving the exploration of surface states in topological semimetals with adsorbates relatively uncharted. This work, based on *ab initio* calculations, examines variations in the topological surface states of MgB₂, a well-known conventional superconductor and topological nodal line semimetal. We employ a thick slab model with Mg/B atoms as surface terminations to simulate its topological surface states. Subsequently, we investigate the adsorption of hydrogen (H), hydroxide (OH), and water (H_2O) on the surface slabs to observe changes in the surface states. The pristine slab model gives the drumhead-like surface states inside the surface projected nodal lines, while the topological surface states change differently after adsorbing H, OH, and H_2O, which can be understood systematically by combining the surface adsorption Gibbs free energy ΔG, surface terminations, and surface charge density distributions. Especially, our findings suggest that the Bader charge transfer value of surface atoms providing topological states is a key indicator for evaluating the variation in topological surface states after adsorption. This study provides a systematic understanding of the topological surface states of MgB₂ with different adsorbates, paving the way for future theoretical and experimental investigations in related fields and shedding light on the potential device applications of topological materials.

Introduction

Topological materials, including topological insulators (TIs),[1] topological superconductors (TSCs),[2,3] and topological semi-metals (TSMs)[4] have been attracting significant research interest in recent years. The study of topological materials starts from the gapped TIs and TSCs, and then extends to gapless TSMs that hold topologically non-trivial band crossing points around the Fermi level (EF). The TSMs can be roughly classified into Weyl semimetals (WSMs)[5–7] holding pairs of two-fold degenerate Weyl points with opposite chirality, Dirac semi-metals (DSMs)[8–10] with four-fold degenerate Dirac points, and

nodal line semimetals (NLSMs) with continuous line of nodes[11–23] inside the first Brillouin zone (BZ). A fascinating property shared by all topological materials is the so-called bulk-boundary correspondence,[1,2] which means if there is non-trivial band topology in the bulk, we can expect topologically protected conducting states on the edge, such as the Dirac cone surface states for TIs,[1] Majorana zero modes (MZMs) for TSCs,[2] surface Fermi arc/loops for WSMs/DSMs,[5,6,10] and drumhead-like surface states inside/outside the projected nodal lines for NLSMs.[14,15] Generally, the topological surface states (TSSs) are topologically protected and robust against perturbations or disorders that do not change the protected symmetries.

Besides the comprehensive theoretical and materials studies, the applications of topological materials still need to be improved. In recent years, there has been a growing interest in investigating the potential use of topological materials for energy conversion and storage,[24] closely related to surface adsorption in electrochemical processes. The earliest *ab initio* calculations on the catalytic properties of topological materials began with the topological insulator bismuth selenide (Bi_2Se_3) covered with a monolayer of

[a] *Key Laboratory of Advanced Functional Materials of Education Ministry of China, Institute of Advanced Energy Materials and Devices, College of Materials Science and Engineering, Beijing University of Technology, Beijing 100124, China. E-mail: wangch33@bjut.edu.cn*

[b] *School of Physics and Optoelectronic Engineering, Shandong University of Technology, Zibo 255000, China. E-mail: bukun94@163.com*

† Electronic supplementary information (ESI) available. See DOI: https://doi.org/10.1039/d4cp02362e

golden (Au) atoms.[25] The concept of "electron baths" was introduced in that work, which suggested that Bi_2Se_3 could not only modulate the adsorption energy of adsorbates, but also endow impart catalytically enhanced performances to the surface of Au atoms by endowing the Dirac cone bands of the topological surface states. Bi_2Se_3-covered monolayer ZnSe exhibited excellent catalytic performance for hydrogen evolution reaction (HER) on the surface.[26] Research by Freitas et al. opens up a novel hydrogenated band gap of XBi (X = B, Al, Ga and In) monolayers, showing interesting electronic behavior in room-temperature applications of these two-dimensional materials.[27] Moreover, Freitas et al. investigated the structural, electronic and topological insulation properties of XBi (X = B, Al, Ga and In) monolayers after halogenation. They lead to chemical tunability, produce apparent band inversion symmetry, and exhibit Rashba-type spin splitting in the valence bands of these systems.[28]

However, the low conductivity of the bulk phases in topological insulators can harm the catalytic kinetics. Given this, researchers have increasingly focused on topological semimetals because of their high chemical stability and relatively elevated conductivity. A series of WSMs (NbP, TaP, NbAs, TaAs, NiSi) were found to be good HER catalysts, and provided both theoretical and experimental evidence that the catalytic enhancement arises from the nontrivial Fermi arc surface states.[29,30] In addition, the magnetic WSM $Co_3Sn_2S_2$ was found to have high oxygen evolution reaction (OER) properties and it was concluded that the surface of bulk $Co_3Sn_2S_2$ is more favorable for OH adsorption due to the presence of topological surface states.[31] For the study of NLSMs, Li et al. first proposed that the TiSi family, which have the stable topologically non-trivial drumhead-like surface states, could serve as a platform for HER catalysis.[32] In 2023, Zhang et al. investigated the HER performance of topological nodal net semimetals by using metal diboride MB_2 (M = Ti, Sc, V, Zr, Hf, Nb, Ta, and Y).[33] They found that the Gibbs free energy of hydrogen adsorption exhibited an excellent linear relationship with the density of states associated with the topological surface bands. For the applications of topological materials in an aqueous environment, exploring the effect of H, OH, and H_2O adsorption on the surfaces of topological materials is necessary. However, previous studies on the surface states of NLSMs mainly focus on the pristine surface case or HER catalytic performance, while a systematical understanding of the variations of topological surface states after adsorbing different substances is still lacking. Generally, for NLSMs, the topological surface states have a strong dependence on the configurations of the surface terminations, and the drumhead-like surface states can be inside/outside the nodal lines when the surface terminations show a zigzag/beard type.[18,20,34] In this work, we perform a systematical ab initio study on the variations of the topological surface states of MgB_2, which is a well-known conventional superconductor with a high critical temperature T_c up to 39 K,[35,36] and also a nodal line semimetal with straight band crossing lines on the edge of the first BZ.[37,38] We build a thick slab model to simulate the topological surface states of MgB_2. For the pristine MgB_2 slab, the slab model gives a drumhead-like topological surface state inside the nodal lines, consistent with ref. 35. Then we add hydrogen (H), hydroxide (OH), and water

(H_2O) onto the slab models to see the variations of the surface states, and the surface states change differently with different surface adsorbates, which can be understood systematically by combining the surface adsorption free energy ΔG, the surface terminations, and the surface charge density distributions. Our work has provided a systematical understanding of the topological surface states of MgB_2 with different surface adsorptions, which will also guide future theoretical studies and device applications of topological materials.

Computational method

We perform the ab initio calculations employing the Vienna Ab initio Simulation Package (VASP).[39] The generalized gradient approximation (GGA) developed by Perdew, Burke, and Ernzerhof (PBE)[40] is used as the exchange–correlation potential. The all-electron projector augmented wave (PAW)[41] method is used and we set a plane-wave basis set with an energy cutoff of 500 eV. The BZ is sampled with an $8 \times 8 \times 10$ Monkhorst–Pack k-point grid for the bulk system, and a $12 \times 12 \times 1$ k-point grid for the slab systems. The vacuum layer of the slab system is set to 30 Å. The geometries are optimized with symmetry constraints until the remaining atomic forces are less than 10^{-5} eV Å^{-1} for the bulk system and 10^{-3} eV Å^{-1} for the slab system. The energy convergence criterion is set to be 10^{-6} eV for the bulk system, and 10^{-5} eV for the slab system. For the further exploration of the topological electronic properties of MgB_2, we have built a tight-binding (TB) model using the maximally localized Wannier functions implemented in the Wannier90 package[42,43] based on the s and p orbitals of Mg and B atoms, and searched all the nodal points and calculated the Berry phases with WannierTools package.[44]

Results and discussion

We firstly present the crystalline structure of MgB_2. Fig. 1(a) shows the unit cell of MgB_2. MgB_2 has a hexagonal unit cell with one Mg atom and two B atoms in $P6/mmm$ symmetry (D_{6h}^1, space group No. 191). The optimized lattice parameters are $a = b = 3.079$ Å, and $c = 3.505$ Å, which are very close to the experimental values $a = b = 3.083$ Å, and $c = 3.521$ Å.[45] The Mg atom occupies the 1a (0,0,0) Wyckoff position, while the B atoms occupy the 2d (2/3,1/3,1/2) Wyckoff positions. Fig. 1(b) shows the first BZ and the projected (010) surface BZ of MgB_2, with some newly defined surface k points $\bar{X}_{0.15}$ (0.5,0.15), $\bar{X}_{0.218}$ (0.5,0.218), $\bar{X}_{0.27}$ (0.5,0.27), $\bar{X}_{0.3}$ (0.5,0.3), $\bar{\Gamma}_{0.15}$ (0.0,0.15), $\bar{\Gamma}_{0.218}$ (0.0,0.218), $\bar{\Gamma}_{0.27}$ (0.0,0.27), and $\bar{\Gamma}_{0.3}$ (0.0,0.3).

We compared the bulk phase band structure of MgB_2 with and without SOC, and found that SOC had almost no effect on the band structure. In Fig. S2 of ESI† (ref. 46). Therefore, SOC was not considered in the subsequent study. Fig. 2(a) depicts the calculated band structures of MgB_2 without considering the spin–orbit coupling (SOC). Here, we see that the bands are all doubly degenerate along the high-symmetric H–K edge, and the degenerate bands are contributed mainly by the p orbitals of B
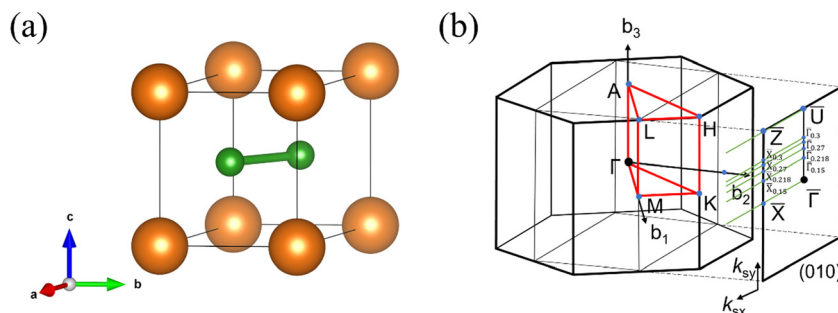
This journal is © the Owner Societies 2024

Phys. Chem. Chem. Phys., 2024, **26**, 23600–23608 | **23601**

Fig. 1 (a) Crystal structure of MgB$_2$ (orange ball: Mg; green ball: B), (b) The first BZ and projected (010) surface BZ of MgB$_2$, with some newly defined surface k points $\bar{X}_{0.15}$ (0.5,0.15), $\bar{X}_{0.218}$ (0.5,0.218), $\bar{X}_{0.27}$ (0.5,0.27), $\bar{X}_{0.3}$ (0.5,0.3), $\bar{\Gamma}_{0.15}$ (0.0,0.15), $\bar{\Gamma}_{0.218}$ (0.0,0.218), $\bar{\Gamma}_{0.27}$ (0.0,0.27), and $\bar{\Gamma}_{0.3}$ (0.0,0.3).

atoms. The detailed band structures analysis in the 3D BZ shows that MgB$_2$ is a topological nodal line semimetal with six equivalent nodal lines along the high-symmetric H–K edges of the first BZ as shown in Fig. 2(b). The TB band structures and the distribution of band crossing nodes are shown in Fig. S1 of the ESI† (ref. 46). To confirm the topological origin of the nodal lines, we selected a closed loop around the nodal line and calculated the accumulated Berry phase ϕ_B, which are defined as:[15]

$$\phi_B = \oint A(k)\mathrm{d}k \qquad (1)$$

$$A(k) = -i \sum_{occ} \langle u_c(k)|\partial k|u_c(k)\rangle \qquad (2)$$

where, $A(k)$ is the Berry connection, $|u_c|(k)\rangle$ is the Bloch wave function, and *occ* denotes the number of occupied bands. The calculated Berry phase is $\phi_B = \pi$, thus confirming the topological origin and the robustness of these nodal lines.

TSSs analysis of multilayer structures are shown in Fig. S3 and S4 of ESI† (ref. 46). The 3-layer, 7-layer, 13-layer and 20-layer slab models are built to calculate the energy band structure, and found that the surface state of band structure reached the stable and clear result after the 13th layer. Considering the saving of computing resources and the improvement of scientific research efficiency, we do not employ the thicker slab than 20-layer. We have calculated (010) surface states of the 20-layer thick slab with Mg/B atoms as surface terminations as shown in Fig. 3. Because we aim to study the effect of adsorption of small

molecules on the topological surface state of MgB$_2$, we draw the distribution of the volume phase nodal lines of MgB$_2$, and find that its topological surface state will appear on surface (010). Fig. 3(a) shows the estimated Mg-terminated surface states along the $\bar{\Gamma}$–$\bar{X}$–$\bar{\Gamma}$, $\bar{\Gamma}_{0.15}$–$\bar{X}_{0.15}$–$\bar{\Gamma}_{0.15}$, $\bar{\Gamma}_{0.218}$–$\bar{X}_{0.218}$–$\bar{\Gamma}_{0.218}$, and $\bar{\Gamma}_{0.3}$–$\bar{X}_{0.3}$–$\bar{\Gamma}_{0.3}$ paths as sketched in Fig. 1(b). The nearly flat topological surface bands are inside the projected nodal lines. Fig. 3(c) shows the Mg-terminated slab model we used and the band decomposed charge density for the topological surface bands at the projected $\bar{X}$ point, which confirms that the topological surface states are indeed from the surface B atoms. Fig. 3(b) shows the surface states given by the B-terminated slab models along the projected $\bar{\Gamma}$–$\bar{X}$–$\bar{\Gamma}$, $\bar{\Gamma}_{0.15}$–$\bar{X}_{0.15}$–$\bar{\Gamma}_{0.15}$, $\bar{\Gamma}_{0.27}$–$\bar{X}_{0.27}$–$\bar{\Gamma}_{0.27}$, and $\bar{\Gamma}_{0.3}$–$\bar{X}_{0.3}$–$\bar{\Gamma}_{0.3}$ paths. The drumhead-like topological surface states can be seen along $\bar{\Gamma}$–$\bar{X}$–$\bar{\Gamma}$ paths, while the topological surface bands tend to merge into the bulk along other paths. Fig. 3(d) gives the B-terminated slab model we used and also the band decomposed charge densities for the topological surface bands at the projected $\bar{X}$ point, also confirming that the topological surface states are indeed contributed by the surface B atoms. Remarkably, in both the Mg/B-terminated cases, the topological surface bands exclusively originate from the surface B atoms, as the bulk bands associated with the nodal lines are contributed by B atoms. Our findings align with those in ref. 37.

Notably, previous studies on the surface states of MgB$_2$ have primarily focused on the pristine case.[37,38] However, the surface adsorption is inevitable in real-world applications of topological
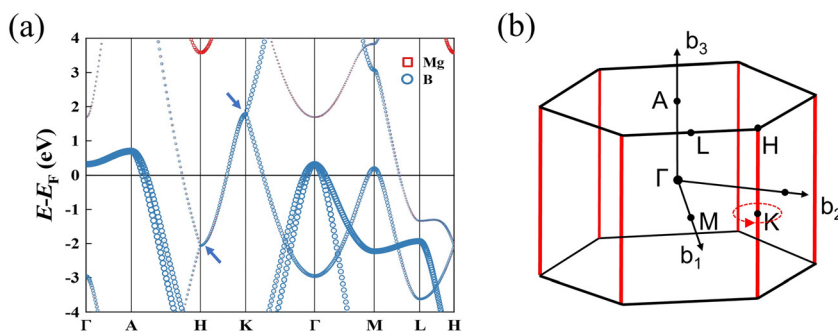

Fig. 2 (a) The calculated band structures of MgB$_2$, the bands are all doubly degenerate along the high-symmetric H–K path without considering the spin–orbit coupling (SOC). The degenerate bands are contributed by B atoms; (b) the nodal lines of MgB$_2$ in the first BZ, which are along the high-symmetric H–K edges (red line). The Berry phase associated with the nodal line is π.

23602 | *Phys. Chem. Chem. Phys.*, 2024, **26**, 23600–23608

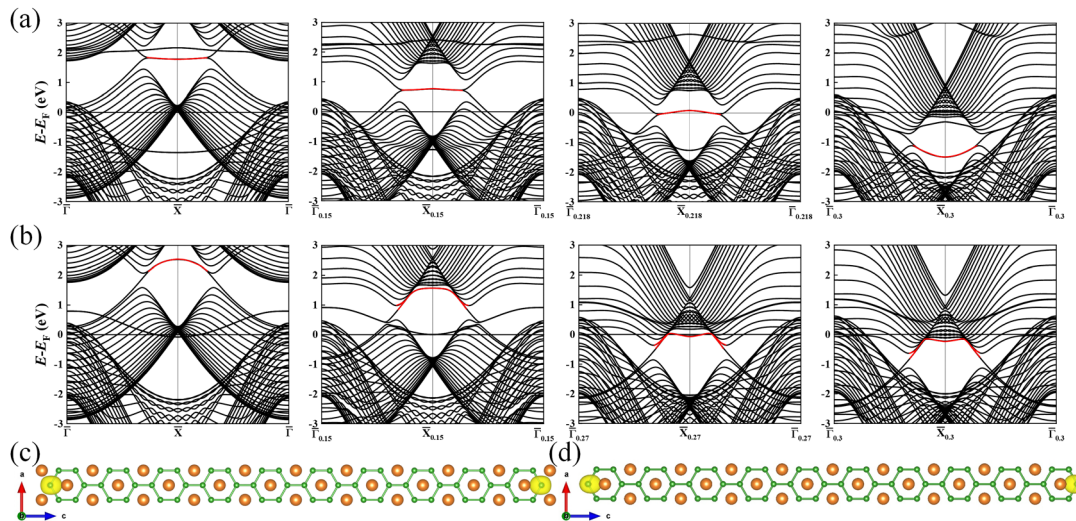This journal is © the Owner Societies 2024

Fig. 3 (a) The Mg-terminated surface states along the projected $\bar{\Gamma}-\bar{X}-\bar{\Gamma}$, $\bar{\Gamma}_{0.15}-\bar{X}_{0.15}-\bar{\Gamma}_{0.15}$, $\bar{\Gamma}_{0.218}-\bar{X}_{0.218}-\bar{\Gamma}_{0.218}$, and $\bar{\Gamma}_{0.3}-\bar{X}_{0.3}-\bar{\Gamma}_{0.3}$ paths; (b) The B-terminated surface states along the projected $\bar{\Gamma}-\bar{X}-\bar{\Gamma}$, $\bar{\Gamma}_{0.15}-\bar{X}_{0.15}-\bar{\Gamma}_{0.15}$, $\bar{\Gamma}_{0.27}-\bar{X}_{0.27}-\bar{\Gamma}_{0.27}$, and $\bar{\Gamma}_{0.3}-\bar{X}_{0.3}-\bar{\Gamma}_{0.3}$ paths; (c) the slab model and the charge density associated with the surface bands for Mg-terminations at the projected $\bar{X}$ point; (d) the slab model and the charge density associated with the surface bands for B-terminations at the projected $\bar{X}$ point. The red line in (a) and (b) represents the drumhead-like topological surface states between two nodal points.

materials, especially in aqueous environments. Therefore, we systematically studied on the variations of the surface states for MgB$_2$ by introducing H, OH, and H$_2$O onto the Mg/B-terminated slab models. In this section, we calculate the surface adsorption Gibbs free energies $\Delta G_{\text{H}^*,\text{OH}^*,\text{H}_2\text{O}^*}$ to determine the most favorable adsorption sites for H, OH, and H$_2$O adsorbed on the Mg/B-terminated slab models according to the following formulas:[47]

$$\Delta G_{\text{H}^*} = \Delta E_{\text{H}^*} + \Delta E_{\text{ZPE}} - T\Delta S \quad (3)$$

$$\Delta E_{\text{H}^*} = \frac{1}{n}\left(E_{\text{slab+H}} - E_{\text{slab}} - \frac{n}{2}E_{\text{H}_2}\right) \quad (4)$$

$$\Delta G_{\text{OH}^*} = \Delta E_{\text{OH}^*} + \Delta E_{\text{ZPE}} - T\Delta S \quad (5)$$

$$\Delta E_{\text{OH}^*} = E_{\text{slab+OH}} - E_{\text{slab}} - E_{\text{H}_2\text{O}} - \frac{1}{2}E_{\text{H}_2} \quad (6)$$

$$\Delta G_{\text{H}_2\text{O}^*} = \Delta E_{\text{H}_2\text{O}^*} + \Delta E_{\text{ZPE}} - T\Delta S \quad (7)$$

$$\Delta E_{\text{H}_2\text{O}^*} = E_{\text{slab+H}_2\text{O}} - E_{\text{slab}} - E_{\text{H}_2\text{O}} \quad (8)$$

where, the * stands for the adsorption site on the surface, $\Delta E_{\text{H}^*,\text{OH}^*,\text{H}_2\text{O}^*}$ means the adsorption energies for H, OH, and

H$_2$O, ΔE_{ZPE} means the difference related to the zero-point energy between the gas phase and the adsorbed state, T is the temperature and ΔS is the change of the entropy.[47] The most favorable adsorption sites and their corresponding adsorption Gibbs free energies are presented in Table 1. Additional details regarding the calculations for alternative sites can be found in the Tables S1–S3 of the ESI† (ref. 46). Notably. The B-terminated slab exhibits a more pronounced adsorption effect on H, OH, and H$_2$O than the Mg-terminated slab. Furthermore, both H and OH exhibit significant negative values of $\Delta G_{\text{H}^*,\text{OH}^*}$, respectively, indicating strong adsorption effects, while the adsorption effect of H$_2$O is relatively weak. Fig. 4 illustrates the Mg/B-terminated slab models adsorbing H, OH, and H$_2$O onto their most favorable adsorption sites. The red dashed line represents the distance from the surface adsorbed atom to the surface atom, with specific distance values provided in Table 1.

Subsequently, we discuss the surface states of the slab model adsorbing H and OH, represented in Fig. 5 and 6, respectively. Fig. 5(a) and 6(a) display the nearly flat drumhead-like topological surface states inside the nodal lines of the Mg-terminated pristine slab model along the projected

Table 1 The most favorable adsorption sites, the bond distance from the surface-adsorbed atom to the surface atom, the corresponding surface adsorption free energies (ΔG), and the charge gain and loss of the surface atoms derived from the Bader charge analysis for the Mg/B-terminated slab adsorbing H, OH, and H$_2$O. "+" denotes a gain of charge, while "−" signifies a loss of charge (unit in e$^-$)

Systems	Adsorbate	Site	Bond distance (Å)	ΔG (eV)	$\Delta\rho$ (e$^-$)		
Mg-terminated slab					Adsorbate	B	Mg
	H	Hole	2.370	−0.319	+0.900	−0.307	−0.011
	OH	Bridge	1.974	−0.347	+0.772	−0.183	−0.182
	H$_2$O	Top	2.124	0.318	+0.224	−0.021	−0.114
B-terminated slab					Adsorbate	B	Mg
	H	Top	1.211	−1.252	+0.361	−0.127	−0.017
	OH	Top	1.352	−1.442	+0.690	−0.228	−0.015
	H$_2$O	Top	1.554	−0.170	+0.266	−0.082	−0.007

This journal is © the Owner Societies 2024

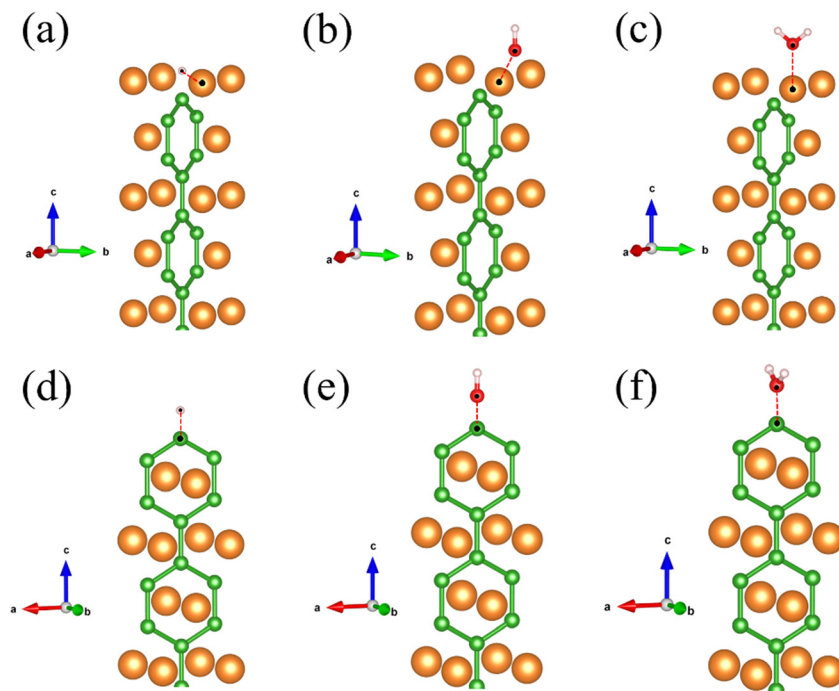Phys. Chem. Chem. Phys., 2024, 26, 23600–23608 | 23603

Fig. 4 (a) Mg-terminated slab adsorbing H on the hole site; (b) Mg-terminated slab adsorbing OH on the bridge site; (c) Mg-terminated slab adsorbing H₂O on the top site; (d) B-terminated slab adsorbing H on the top site; (e) B-terminated slab adsorbing OH on the top site; (f) B-terminated slab adsorbing H₂O on the top site. The red dashed lines represent the distance from the surface adsorbed atom to the surface atom, and the distance values are shown in Table 1.

$\bar{\Gamma}$–$\bar{X}$–$\bar{\Gamma}$ direction. Fig. 5(b) and 6(b) show the surface states adsorbing H and OH to the slab model on a single side, respectively, breaking the inversion symmetry of the slab model. Thus, the energy of one surface band is lower since the surface dangling bonds are saturated while another surface band is still there. Here, we propose ΔE_{TSS} as an index to describe the disturbance of adsorbates to the topological surface states, which is defined as:

$$\Delta E_{TSS} = \Delta E_{TSS_{Ads}} - \Delta E_{TSS_0} \tag{9}$$
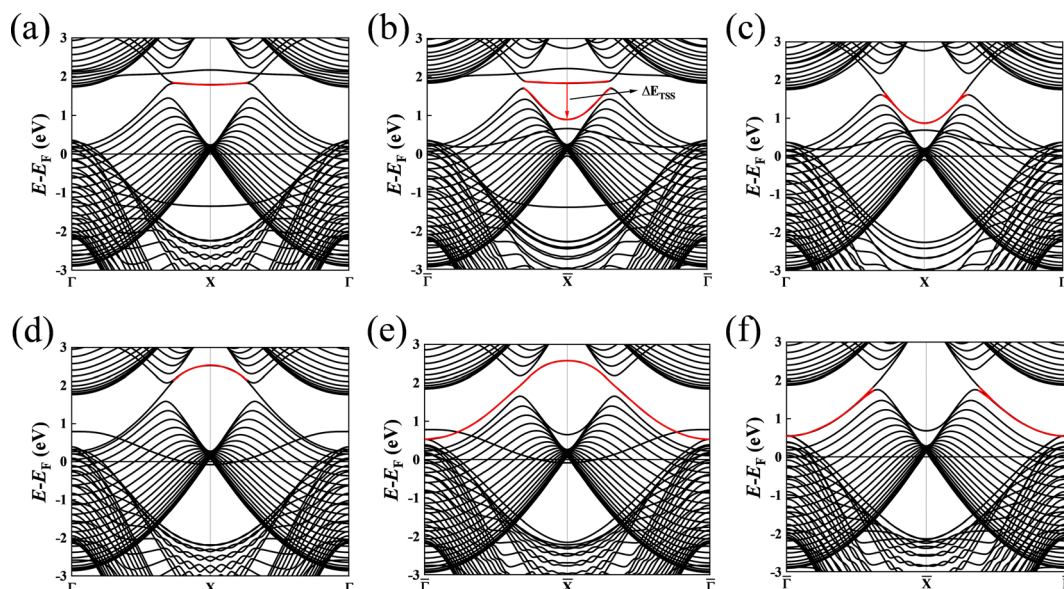

Fig. 5 (a) The (010) surface states from the pristine Mg-terminated slab; (b) the (010) surface states from the Mg-terminated slab adsorbing H on a single side; (c) the (010) surface states from the Mg-terminated slab adsorbing H on both sides; (d) the (010) surface states from the pristine B-terminated slab; (e) the (010) surface states from the B-terminated slab adsorbing H on a single side; (f) the (010) surface states from the B-terminated slab adsorbing H on both sides. The red line indicates the drumhead-like topological surface states between two nodal points.
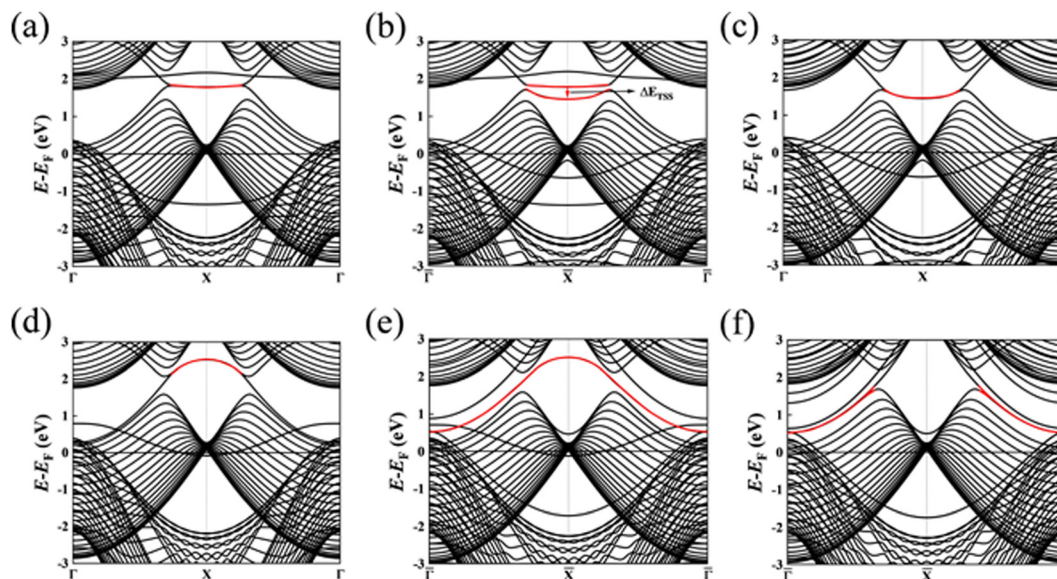
23604 | *Phys. Chem. Chem. Phys.*, 2024, **26**, 23600–23608

This journal is © the Owner Societies 2024

Fig. 6 (a) The (010) surface states from the pristine Mg-terminated slab; (b) the (010) surface states from the Mg-terminated slab adsorbing OH on a single side; (c) the (010) surface states from the Mg-terminated slab adsorbing OH on both sides; (d) the (010) surface states from the pristine B-terminated slab; (e) the (010) surface states from the B-terminated slab adsorbing OH on a single side; (f) the (010) surface states from the B-terminated slab adsorbing OH on both sides. The red line indicates the drumhead-like topological surface states between two nodal points.

Where the $E_{TSS_{Ads}}$ is the energy of the topological surface state of the slab with adsorbate at the projected $\bar{X}$ point, E_{TSS_0} means the topological surface state energy of pristine slab at the projected $\bar{X}$ point. In addition, Table 1 displays the ΔE_{TSS} values. It is evident that ΔE_{TSS} in Fig. 5(b) has a more negative value (-0.936 eV) compared to Fig. 6(b) (-0.322 eV). This fact indicates that the H has a more significant impact on the topological surface state on Mg-terminated slab than OH. Fig. 5(c) and 6(c) depict the surface states with H and OH adsorbed on both sides of the slab model. The inversion symmetry of the slab model is restored, causing the surface bands are degenerate with lower energies. The changes in surface state energy in Fig. 5(c) are more significant than those in Fig. 6(c). In both cases, the surface states remain within the nodal lines. This is because the surface B atoms primarily contribute to the topological surface states. Adding H and OH atoms onto Mg atoms does not drastically alter the topological band structures contributed by the B atoms.

Fig. 5(d) and 6(d) illustrate the surface states with the B-terminated pristine slab model along the projected $\bar{\Gamma}-\bar{X}-\bar{\Gamma}$ direction. These figures reveal the presence of nearly flat drumhead-like topological surface states situated within the nodal lines. Additionally, Fig. 5(e) and 6(e) showcase the surface states of the B-terminated slab with the adsorbates H and OH on a single side, respectively, breaking the inversion symmetry of the slab model. It is worth noting that the surface states are present inside and outside the nodal lines. This observation indicates a substantial alteration in the topological band structure resulting from the strong interaction between B atoms and H/OH. Fig. 5(f) and 6(f) show the surface states of B-terminated slab with the adsorbates H or OH on both sides, where the inversion symmetry of the slab model is restored,

and the surface states are outside the nodal lines. Since B atoms mainly contribute to the topological surface states, adding H/OH onto B atoms changes the surface terminations from zigzag to beard types. This leads to the surface states outside the nodal lines, consistent with the previous works.[18,20,34] Fig. S2 and S3 of the ESI† (ref. 46) show the determination of the surface state positions in the band analysis.

We also discuss the surface states of the slab model adsorbing H_2O. Fig. 7(a) depicts the surface states from the Mg-terminated pristine slab model along the projected $\bar{\Gamma}-\bar{X}-\bar{\Gamma}$ direction as a reference. Fig. 7(b) illustrates the surface states when H_2O is adsorbed onto a single side of the slab model, breaking the inversion symmetry of the slab model. Notably, the two surface bands exhibit a considerably weaker splitting compared to cases involving the adsorption of H/OH. The Mg-terminated slab shows a weak adsorption of H_2O with the positive ΔG of 0.318 eV. Fig. 7(c) shows the surface states adsorbing H_2O to the slab model on both sides, where the inversion symmetry of the slab model is restored and the surface bands are degenerate. Moreover, the topological surface bands also change slightly compared to the Fig. 7(a). Fig. 7(d) shows the surface states with a B-terminated pristine slab model along the projected $\bar{\Gamma}-\bar{X}-\bar{\Gamma}$ direction as a benchmark and the nearly flat drumhead-like topological surface states can be seen inside the nodal lines. Fig. 7(e) shows the surface states adsorbing H_2O to the slab model on a single side, breaking the inversion symmetry of the slab model. Notably though the H_2O interacts with the B-terminated surface directly, H_2O is a charge neutral molecule and the B-terminated surfaces show a very weak adsorption to it, the topological surface are states still inside the nodal lines. Fig. 7(f) shows the surface adsorbing H_2O to the slab model on both sides, the inversion symmetry of

This journal is © the Owner Societies 2024

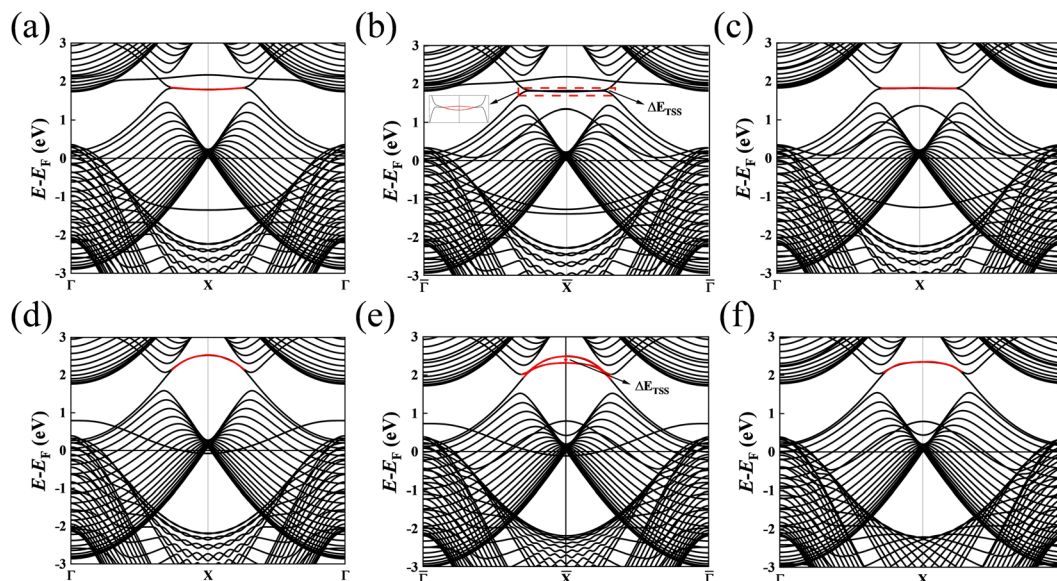*Phys. Chem. Chem. Phys.*, 2024, **26**, 23600–23608 | **23605**

Fig. 7 (a) The (010) surface states given by the pristine Mg-terminated slab; (b) the (010) surface states exhibited by the Mg-terminated slab adsorbing H_2O on a single side; (c) the (010) surface states shown by the Mg-terminated slab upon H_2O adsorption on both sides; (d) the (010) surface states shown by the pristine B-terminated slab; (e) the (010) surface states displayed by the B-terminated slab following H_2O adsorption on a single side; (f) the (010) surface states are depicted by the B-terminated slab after H_2O adsorption on both sides. The red line represents the drumhead-like topological surface states between two nodal points.

the slab model is restored, and the surface bands are degenerate. Also, the surface bands change slightly compared with Fig. 7(d). In either case, the topological surface states are always inside the nodal lines since H_2O is electric neutrality molecule and the surface slab has very weak adsorption for H_2O. The determination of the surface states' position is shown in Fig. S4 of ESI† (ref. 46).

From the results of the topological surface states changes ΔE_{TSS} of MgB_2 with different adsorbates, we expect to propose a critical indicator with a positive correlation with the ΔE_{TSS}. Table 1 presents our calculations of Bader charge analysis[48–51] to show the charge gain and loss of the surface atoms. It is evident that adsorbates H, OH, and H_2O gain electrons, while the surface Mg/B-atoms tend to lose them. Simultaneously, the surface differential charge density calculations reveal this phenomenon, as depicted in Fig. S5 of the ESI† (ref. 46). It is noteworthy that there is a significant positive correlation between the Bader charge transfer of surface B atoms and the ΔE_{TSS}. We further investigated the relationship between the other significant parameters of surface adsorption, such as the bond lengths and adsorption Gibbs free energy, with the ΔE_{TSS}. However, they have a poor correlation, as illustrated in Fig. S6 of the ESI† (ref. 46). Thus, we can infer that the Bader charge transfer value of the surface atoms that provide the topological state is a crucial indicator for evaluating the variation in topological surface states after adsorption.

MgB_2 after adding hydrogen (H), hydroxide (OH), and water (H_2O). The most stable adsorption sites have been identified by calculating the surface adsorption free energies $\Delta G_{H^*,OH^*,H_2O^*}$. Meanwhile, it is shown that either Mg- or B-terminated surface has a very strong adsorption for OH, and then H, while has only weak adsorption for H_2O, and the surface states have a crucial change after the adsorption for H, less change after the adsorption for OH, and only very slight change after the adsorption for H_2O, which can be understood systematically by combining the surface adsorption free energies $\Delta G_{H^*,OH^*,H_2O^*}$, surface terminations, and surface charge density distributions. Particularly, we propose the value of the band structural change of topological surface state ΔE_{TSS} as an index to describe the disturbance of adsorbates to the topological surface states. Analyzing the relationships among Bader charge transfer, adsorption Gibbs free energy, and bond length to ΔE_{TSS}, we observed a high correlation solely between ΔE_{TSS} and the Bader charge transfer of the surface B atoms. The Bader charge transfer value of the surface B atoms providing the topological state should be a key indicator for evaluating the variation in topological surface states after adsorbing H, OH, and H_2O adsorbates. Our work has provided a systematical understanding on the variation of topological surface states after surface adsorptions, and will also pave the way for future studies on the device applications of topological materials.

Conclusion

In summary, we have performed by *ab initio* calculations a systematical study on the variation of the (010) surface states of

Data availability

The data supporting this article have been included as part of the ESI.†

23606 | *Phys. Chem. Chem. Phys.*, 2024, **26**, 23600–23608

This journal is © the Owner Societies 2024

Conflicts of interest

There are no conflicts to declare.

Acknowledgements

References

1 M. Z. Hasan and C. L. Kane, Colloquium:Topological insulators, *Rev. Mod. Phys.*, 2010, **82**, 3045.

2 X. L. Qi and S. C. Zhang, Topological insulators and superconductors, *Rev. Mod. Phys.*, 2011, **83**, 1057.

3 C. K. Chiu, J. C. Y. Teo, A. P. Schnyder and S. Ryu, Classification of topological quantum matter with symmetries, *Rev. Mod. Phys.*, 2016, **88**, 035005.

4 N. P. Armitage, E. J. Mele and A. Vishwanath, Weyl and Dirac semimetals in three-dimensional solids, *Rev. Mod. Phys.*, 2018, **90**, 015001.

5 X. Wan, A. M. Turner, A. Vishwanath and S. Y. Savrasov, Topological semimetal and Fermi-arc surface states in the electronic structure of pyrochlore iridates, *Phys. Rev. B: Condens. Matter Mater. Phys.*, 2011, **83**, 205101.

6 H. Weng, C. Fang, Z. Fang, B. Andrei. Bernevig and X. Dai, Weyl Semimetal Phase in Noncentrosymmetric Transition-Metal Monophosphides, *Phys. Rev. X*, 2015, **5**, 011029.

7 G. Xu, H. Weng, Z. Wang, X. Dai and Z. Fang, Chern Semimetal and the Quantized Anomalous Hall Effect in $HgCr_2Se_4$, *Phys. Rev. Lett.*, 2011, **107**, 186806.

8 Z. Wang, Y. Sun, X. Q. Chen, C. Franchini, G. Xu, H. Weng, X. Dai and Z. Fang, Dirac semimetal and topological phase transitions in A_3Bi (A = Na, K, Rb), *Phys. Rev. B: Condens. Matter Mater. Phys.*, 2012, **85**, 195320.

9 Z. Wang, H. Weng, Q. Wu, X. Dai and Z. Fang, Three dimensional Dirac semimetal and quantum transport in Cd_3As_2, *Phys. Rev. B: Condens. Matter Mater. Phys.*, 2013, **88**, 125427.

10 Q. D. Gibson, L. M. Schoop, L. Muechler, L. S. Xie, M. Hirschberger, N. P. Ong, R. Car and R. J. Cava, Three-dimensional Dirac semimetals: Design principles and predictions of new materials, *Phys. Rev. B: Condens. Matter Mater. Phys.*, 2015, **91**, 205128.

11 M. Phillips and V. Aji, Tunable line node semimetals, *Phys. Rev. B: Condens. Matter Mater. Phys.*, 2014, **90**, 115111.

12 Y. Kim, B. J. Wieder, C. L. Kane and A. M. Rappe, Dirac line nodes in inversion-symmetric crystals, *Phys. Rev. Lett.*, 2015, **115**, 036806.

13 R. Yu, H. Weng, Z. Fang, X. Dai and X. Hu, Topological node-line semimetal and Dirac semimetal state in antiperovskite Cu_3PdN, *Phys. Rev. Lett.*, 2015, **115**, 036807.

14 C. Fang, Y. Chen, H. Y. Kee and L. Fu, Topological nodal line semimetals with and without spin-orbital coupling, *Phys. Rev. B: Condens. Matter Mater. Phys.*, 2015, **92**, 081201(R).

15 C. Fang, H. Weng, X. Dai and Z. Fang, Topological nodal line semimetals, *Chin. Phys. B*, 2016, **25**, 117106.

16 Q. Xu, R. Yu, Z. Fang, X. Dai and H. Weng, Topological nodal line semimetals in the CaP_3 family of materials, *Phys. Rev. B*, 2017, **95**, 045136.

17 K. Bu, J. T. Wang, H. Weng and C. Chen, Topological semimetal in an sp^2-sp^3 hybridized carbon network with nodal rings, *Phys. Rev. B*, 2020, **101**, 205104.

18 K. Bu, Y. Qian, J. T. Wang and H. Weng, Hybrid Nodal Chain in an Orthorhombic Graphene Network, *Phys. Rev. B*, 2021, **103**, L081108.

19 M. R. Khan, K. Bu and J. T. Wang, Topological nodal line semimetal in an all-sp^2 monoclinic carbon, *New J. Phys.*, 2022, **24**, 043007.

20 Y. Tao, K. Bu and J. T. Wang, Orthorhombic C_{32}: A topological semimetal with nodal ring, *Phys. Lett. A*, 2022, **451**, 128397.

21 J. T. Wang, K. Bu, Y. Qian, H. Weng and C. F. Chen, Pentagraphite C_8: An all-sp^2 topological nodal-line semimetal, *Phys. Rev. B*, 2021, **104**, 245143.

22 K. Bu and J. T. Wang, Topological nodal line semimetal with large nodal ring in an all-sp^2 hybridized carbon network formed by all-ten-membered carbon rings, *Phys. Rev. B*, 2023, **107**, 245111.

23 K. Bu and J. T. Wang, Topological states in the polymerized carbon nanotubes, *Phys. Lett. A*, 2023, **480**, 128396.

24 H. Luo, P. Yu, G. Li and K. Yan, Topological quantum materials for energy conversion and storage, *Nat. Rev. Phys.*, 2022, **4**, 611.

25 H. Chen, W. Zhu, D. Xiao and Z. Zhang, CO oxidation facilitated by robust surface states on Au-covered topological insulators, *Phys. Rev. Lett.*, 2011, **107**, 056804.

26 L. Li, J. Zeng, W. Qin, P. Cui and Z. Zhang, Tuning the hydrogen activation reactivity on topological insulator heterostructures, *Nano Energy*, 2019, **58**, 40.

27 R. R. Q. Freitas, R. Rivelino, F. de Brito Mota, C. M. C. de Castilho, A. Kakanakova-Georgieva and G. K. Gueorguiev, Topological Insulating Phases in Two-Dimensional Bismuth-Containing Single Layers Preserved by Hydrogenation, *J. Phys. Chem. C*, 2015, **119**, 23599.

28 R. R. Q. Freitas, F. de Brito Mota, R. Rivelino, C. M. C. de Castilho, A. Kakanakova-Georgieva and G. K. Gueorguiev, Tuning band inversion symmetry of buckled III-Bi sheets by halogenation, *Nanotechnology*, 2016, **27**, 055704.

29 C. R. Rajamathi, U. Gupta, N. Kumar, H. Yang, Y. Sun, V. Süß, C. Shekhar, M. Schmidt, H. Blumtritt, P. Werner, B. H. Yan, S. Parkin, C. Felser and C. N. R. Rao, Weyl Semimetals as Hydrogen Evolution Catalysts, *Adv. Mater.*, 2017, **29**, 1606202.

30 W. Liu, X. Zhang, W. Meng, Y. Liu, X. Dai and G. Liu, Theoretical realization of hybrid Weyl state and associated

This journal is © the Owner Societies 2024

Phys. Chem. Chem. Phys., 2024, **26**, 23600–23608 | **23607**

high catalytic performance for hydrogen evolution in NiSi, *iScience*, 2022, **25**, 103543.

31 G. Li, Q. Xu, W. Shi, C. Fu, L. Jiao, M. E. Kamminga, M. Yu, H. Tüysüz, N. Kumar, V. Süß, R. Saha, A. K. Srivastava, S. Wirth, G. Auffermann, J. Gooth, S. Parkin, Y. Sun, E. Liu and C. Felser, Surface states in bulk single crystal of topological semimetal $Co_3Sn_2S_2$ toward water oxidation, *Sci. Adv.*, 2019, **5**, eaaw9867.

32 J. Li, H. Ma, Q. Xie, S. Feng, S. Ullah, R. Li, J. Dong, D. Li, Y. Li and X. Q. Chen, Topological quantum catalyst: Dirac nodal line states and a potential electrocatalyst of hydrogen evolution in the TiSi family, *Sci. China Mater.*, 2018, **61**, 23.

33 X. Zhang, L. Wang, M. Li, W. Meng, Y. Liu, X. Dai, G. Liu, Y. Gu, J. Liu and L. Kou, Topological surface state: Universal catalytic descriptor in topological catalysis, *Mater. Today*, 2023, **67**, 23.

34 S. Ryu and Y. Hatsugai, Topological Origin of Zero-Energy Edge States in Particle-Hole Symmetric Systems, *Phys. Rev. Lett.*, 2002, **89**, 077002.

35 J. Nagamatsu, N. Nakagawa, T. Muranaka, Y. Zenitani and J. Akimitsu, Superconductivity at 39 K in magnesium diboride, *Nature*, 2001, **410**, 63.

36 C. Buzea and T. Yamashita, Review of the superconducting properties of MgB_2, *Supercond. Sci. Technol.*, 2001, **14**, R115.

37 K. H. Jin, H. Huang, J. W. Mei, Z. Liu, L. K. Lim and F. Liu, Topological superconducting phase in high Tc superconductor MgB_2 with Dirac nodal-line fermions, *npj Comput. Mater.*, 2019, **5**, 57.

38 X. Zhou, K. N. Gordon, K. H. Jin, H. Li, D. Narayan, H. Zhao, H. Zheng, H. Huang, G. Cao, N. D. Zhigadlo, F. Liu and D. S. Dessau, Observation of topological surface states in the high-temperature superconductor MgB_2, *Phys. Rev. B*, 2019, **100**, 184511.

39 G. Kresse and J. Furthüller, Effcient iterative schemes for ab initio total-energy calculations using a plane-wave basis set, *Phys. Rev. B: Condens. Matter Mater. Phys.*, 1996, **54**, 11169.

40 J. P. Perdew, K. Burke and M. Ernzerhof, Generalized gradient approximation made simple, *Phys. Rev. Lett.*, 1996, **77**, 3865.

41 P. E. Blöchl, Projector augmented-wave method, *Phys. Rev. B: Condens. Matter Mater. Phys.*, 1994, **50**, 17953.

42 A. A. Mostofi, J. R. Yates, Y. S. Lee, I. Souza, D. Vanderbilt and N. Marzari, Wannier90: A tool for obtaining maximally-localised Wannier functions, *Comput. Phys. Commun.*, 2008, **178**, 685.

43 N. Marzari, A. A. Mostofi, J. R. Yates, I. Souza and D. Vanderbilt, Maximally localized Wannier functions:Theory and applications, *Rev. Mod. Phys.*, 2012, **84**, 1419.

44 Q. S. Wu, S. N. Zhang, H. F. Song, M. Troyer and A. A. Soluyanov, WannierTools: An open-source software package for novel topological materials, *Comput. Phys. Commun.*, 2018, **224**, 405.

45 A. Jain, S. P. Ong, G. Hautier, W. Chen, W. D. Richards, S. Dacek, S. Cholia, D. Gunter, D. Skinner, G. Ceder and K. A. Persson, The Materials Project: A materials genome approach to accelerating materials innovation, *APL Mater.*, 2013, **1**, 011002.

46 See the Supplemental Materials for (1) the Wannier tight-binding model for MgB2; (2) the surface adsorption Gibbs free energies at all possible adsorption sites; (3) Fatband analysis for slab adsorbing H, OH, and H2O; (4) Differential charge density for most favorable adsorption sites; The Supplemental Materials include ref. 40 and 41.

47 K. L. Zhou, Z. Wang, C. B. Han, X. Ke, C. Wang, Y. Jin, Q. Zhang, J. Liu, H. Wang and H. Yan, Platinum single-atom catalyst coupled with transition metal/metal oxide heterostructure for accelerating alkaline hydrogen evolution reaction, *Nat. Commun.*, 2021, **12**, 3783.

48 W. Tang, E. Sanville and G. Henkelman, A grid-based Bader analysis algorithm without lattice bias, *J. Phys.: Condens. Matter*, 2009, **21**, 084204.

49 E. Sanville, S. D. Kenny, R. Smith and G. Henkelman, An improved grid-based algorithm for Bader charge allocation, *J. Comp. Chem.*, 2007, **28**, 899.

50 G. Henkelman, A. Arnaldsson and H. Jónsson, A fast and robust algorithm for Bader decomposition of charge density, *Comput. Mater. Sci.*, 2006, **36**, 354.

51 M. Yu and D. R. Trinkle, Accurate and efficient algorithm for Bader charge integration, *J. Chem. Phys.*, 2011, **134**, 064111.